rf simulation of niobium grains and peak magnetic field enhancement

Guillaume Ferrand,* Claire Z. Antoine, and Sadio Sy Savane
Université Paris-Saclay, CEA, Département des Accélérateurs, de la Cryogénie et du Magnétisme, 91191, Gif-sur-Yvette, France

(Received 23 November 2022; accepted 2 May 2023; published 30 October 2023)

Niobium superconducting cavity performances are limited by the quench magnetic field of niobium. Maximum achievable accelerating field is estimated by simulation during the conception phase. The full geometry of the cavity is implemented but no roughness is taken into consideration. However, several experiences showed that the roughness can increase locally the magnetic field, leading to an effective peak magnetic field on the surface higher than expected by simulation. It can be at the origin of premature quench. The present article presents simulations of grains and defects with different sizes and its effect on the local magnetic peak field. The values implemented in the model are taken from actual surface measurements made by confocal microscopy on representative Nb samples prepared with usual surface treatments. Cut-out of fabrication defects and some thin films have been also explored. As expected, the mean roughness brought by usual chemical polishing as well as electropolishing surface treatment does not increase significantly the local field. But calculation based on actual values sometimes encountered in the surface measurement, or on specific defects, can reach very high field enhancement and can explain premature quench on some cavities within an otherwise good performing production batch.

DOI: 10.1103/PhysRevAccelBeams.26.103102

I. INTRODUCTION

Commissariat à l'Energie Atomique et aux Energies Alternatives, Saclay, France (CEA) is one of the major manufacturers of niobium cavities through projects like Spiral 2, IFMIF, ESS, or Saraf-Phase 2. We developed different shapes of cavities, quarter wave, half wave, and elliptic cavities. All these cavities were designed and simulated, mainly with the HFSS software (Ansys Electromagnetic Desktop). Three main parameters are checked before manufacturing. They are as follows: (i) The cryogenic power consumption (surface resistance multiplied by the magnetic field, integrated over the whole surface). (ii) The peak electric field, in order to limit the risk of field emission. (iii) The peak magnetic field, in order to limit the risk of quench.

However, these simulations are done considering a perfect surface: no roughness, no defect, no dust, no inclusion, etc. In order to take into account these "defects" of the surface, one adds margins on peak fields. In operation, we can easily observe that, from one cavity to another one, the accelerating field at quench can significantly vary, but the actual origin is difficult to assess.

*guillaume.ferrand@cea.fr

A better understanding of the effect of roughness would allow a better definition of the margin to consider and also provide some guidance for the fabrication tolerances.

The morphology at the surface of the grains tends to modify locally the magnetic field. One knows that sharp edges tend to increase the magnetic field, especially if the magnetic field is perpendicular to the edge [1]. Consequently, if edges can increase locally the magnetic field, they can significantly decrease the maximal achievable accelerating field in the cavity.

Surface morphology is related mostly to surface preparation and initial grain size. Other defects like etching pits or accidental fabrication defects can also generate morphologic defects. We wanted to verify this aspect by simulation with simple models, but representative of the surface morphology actually observed on the real material. We wish to provide practical orders of magnitude field enhancements risks on a very practical scale.

In this article, we wanted to focus on the effect of the grain shape of the niobium. Depending on the type of niobium, raw, partially or fully recrystallized, cold-worked, etc., the size of the grain can vary from a few tens of microns to almost the size of the cavity. Second, depending on the surface treatment, the grains are more or less protruding and sharp, resulting in the final surface roughness.

A. Ultimate limits of superconducting rf cavities

SRF cavities need to operate in the Meissner state. When the field is parallel to the surface, the existence of the

Bean-Livingston barrier favors the persistence of the Meissner state above the first critical field of Nb up to the so-called superheated state H_{SH}. The value of H_{SH} for Nb has been calculated in the dirty limit (∼160 mT at 2 K) [2,3] and evaluated by extra polling Ginzburg-Landau results at $T \ll T_C$ for the clean limit (∼240 mT at 0 K) [4].

Best cavities achieve surface field ∼200 mT at ∼2 K [5–9], which is above the H_{C1} of Nb (∼170 mT at 2K) and H_{SH} in the dirty limit, but below H_{SH} in the clean limit.

Most of the time though, in the presence of defects, early penetration of the vortex is observed and the superheating field cannot be maintained [9–12]. Moreover, in the presence of a geometrical defect, the surface barrier is locally suppressed, field is no more parallel to the surface [13], and thus the ultimate limit is expected to be closer to H_{C1} [14]. Anyway, we want to explore here the possible role of morphologic defects in the early quench of cavities, at applied fields much lower than H_{C1}.

B. Previous work on surface morphology

The first insight on roughness was proposed by Knobloch *et al.* in 1999 [15], who explored its possible role in high field Q slope. The fact that baking changes the Q slope without affecting the roughness ruled out this explanation. Saito also explored magnetic field enhancement *a posteriori*, evaluating the global roughness from the experimental curves Q vs E_{acc} [12]. One of us developed a replica technique and explored surface morphology as a possible source of quench, in particular, in the heat affected zone close to the welding seam [1,16]. Since then, several studies of the inner surfaces have identified quench inducing defects, in particular, etching pits [17–21]

Between 2005 and 2010, several labs have run some modeling showing that isolated "bumps" as well as "pits" produce a very large local field enhancement [22–26]. In [27], Kubo proposes an analytical calculation of the field enhancement by applying Maxwell equations for a simplified pit shape. In principle, the approximation is better defined in this analytical case, but the method is quite heavy.

A thorough study of surface topology was conducted at Jlab via power spectral density (see, e.g., [28,29]). Xu *et al.* have performed a 2D simulation of losses derived from topography data [30]. They have tried to introduce the time dependence over an rf period, taking into account the duration where the surface is actually above T_C and then introduced thermal aspects (which occur much slower) to evaluate the surface resistance or Q_0 of cavities exhibiting similar surface state. They applied their method to compare EP vs BCP-treated surfaces and find that BCP shows a strong increase in surface resistance when H_{peak} reaches 80 mT. Comparison with real cavity results shows that the model seems slightly overestimating the surface resistance.

In [31], Morozumi makes a model of an actual defect as measured on a surface replica by laser height mapping (similar to what we measure in the present work with confocal microscopy). The height plot must be converted into a polygon mesh covering the points cloud, the surface must be fitted to form a solidlike surface, and then meshed before calculating the local magnetic field. The field enhancement factor of that particular case was 1.5.

We have tried a similar approach but noted that the results were very sensitive to the smoothing function used to generate a continuous surface (not published here). In order to get quick and practical comparison values, we decided to propose a simpler model, yet based on realistic values (see below).

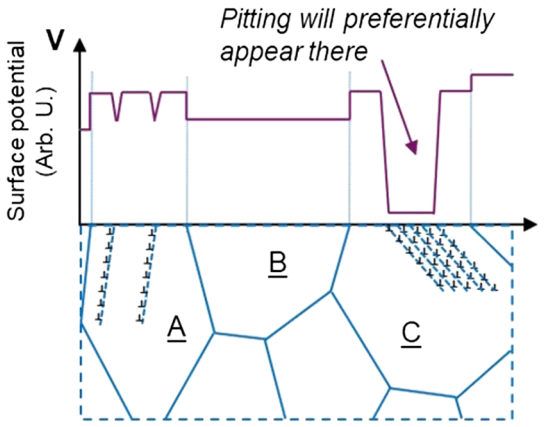

FIG. 1. Variation of the surface potential on a polycrystalline sample. A, B, C refer to different crystalline orientations. In presence of dislocations pile-ups, which induce strong decrease in the local surface potential, additional pitting can be observed (figure after [32]).

C. Origin of the surface morphology

Generally, the roughness is far higher for cavities treated with buffered chemical polishing (BCP), as BCP etches preferentially the defects with lower surface energy and attacks different crystalline orientations at different rates, revealing crystalline facets with sharp angles (see Fig. 1).

Another important aspect is the apparition of etching pits which are often related to local accumulation of dislocations. Dislocations originate from remnant stress such as encountered if the damage layer has been insufficiently removed [33,34] or if thermal stresses are still present in the heat affected zone [19,32,35,36].

The roughness is lower for electropolishing (EP), because, in principle, the limiting mechanism is the diffusion of the Nb ions through a viscous layer, rather than etching [37]. In ideal conditions, mirrorlike surface can be achieved, but for long EP treatment inside cavities, some roughness is retained, although the edges are much smoother than for BCP surfaces (see Fig. 2).

II. REALISTIC SURFACES

Samples of SRF grade, annealed (1000°C, 2 h), and EB-welded niobium have been explored with an optical

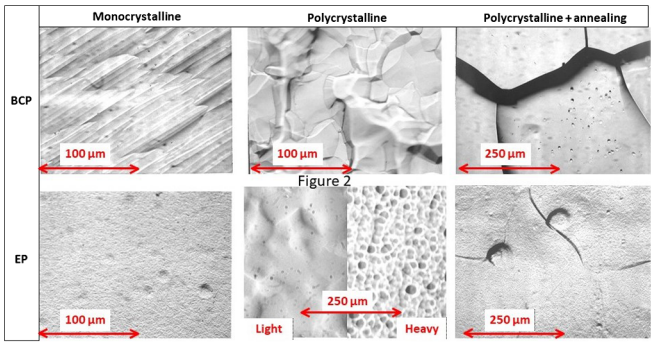

FIG. 2. Optical microscopy showing the various surface aspects after buffered chemical polishing (BCP) or electropolishing (EP). Observed features depend on the type of surface treatment but also on the crystalline characteristics.

microscope, and their roughness parameters have been assessed with a Keyence VK200 confocal microscope images and analyzed with the VK-analyzer software.

Values chosen for simulation are presented in Table I. So-called realistic values have been extracted from roughness measurements (typical Sq) for three categories of Nb: fine grain (typical diameter 70 µm); 1000°C, 2 h, annealed material (typical diameter 500 µm), and thermally affected zone close to the weld (TAZ) (typical diameter 2000 µm). The mean curvature radius has been determined with an ellipse 3 dots intersection method included in the VK-analyzer software and described in Fig. 3.

TABLE I. Morphologic parameter selected for the modeling, based on realistic mean values measured on actual samples. Values marked with a * show the worst-case scenario based on punctually observed values. D = Diameter, T = Thickness, R = Curvature radius on the edge.

Surface treatment		D (µm)	T (µm)	R (µm)	D/T
BCP	Fine grain	70	150*	20	0.5
			10	3*	7
			10	20	7
	Annealed	500	70*	400	7
			15	70*	33
			15	400	33
	TAZ	1000	80*	900	12
			8	30*	125
			8	900	125
	Welding defect	1000	370	40	2.7
EP	Fine grain	70	2*	300	35
			0.5	30*	140
			0.5	300	140
	TAZ	1000	60*	2000	17
			1	50*	1000
			1	2000	1000
	Etching pit	200	20	10	10
Thin film	Nb/Cu (CERN)	0.1	0.05	3	2
Thin film	Nb_3Sn (Cornell)	4	0.4	0.4	10

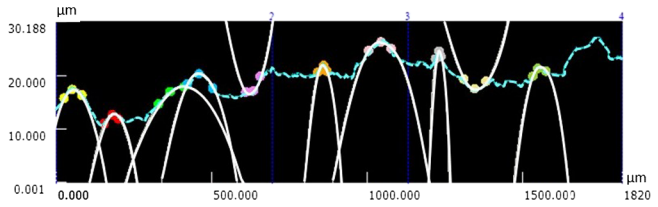

FIG. 3. Example of the method of curvature radius evaluation, here on an EP, fine grain profile.

Besides mean values, "extreme" situations have also been taken into consideration; for instance, instead of the medium peak to valley value Sq, the maximum value Sz has been applied. Instead of the mean curvature radius, the smallest measured value has been implemented, in order to estimate a variation margin.

In addition this roughness consideration, we also have tried to model "real" defects: (i) An etching pit observed on a fine grain EP surface (such pit is often observed if the remaining strain has been left in the material, as explained in Fig. 1). See Fig. 4. (ii) A welding misalignment observed after BCP on a Saraf cavity and associated with an early quench (see Fig. 5). (iii) Deposited thin film. At a large scale, the thin film repeats the morphology of the substrate, but at a smaller scale, roughness due to the growth of the films with very small grains needs to be considered. Two samples have been measured to provide field enhancement indications but are not meant to represent statistically all thin films.

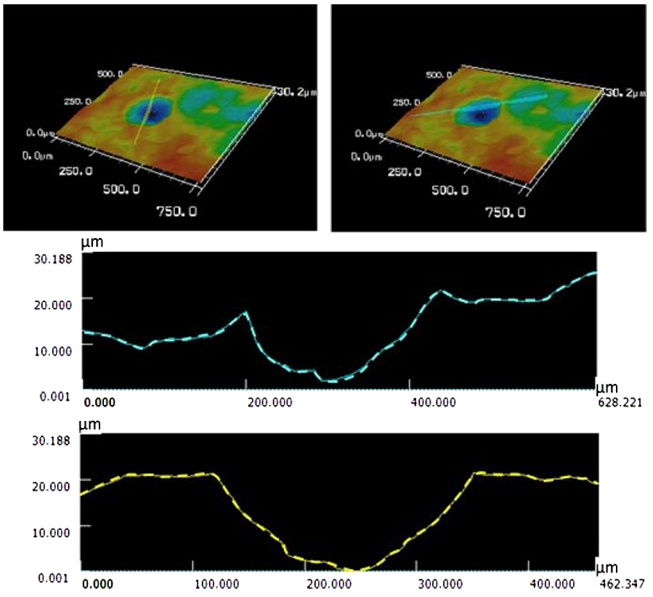

FIG. 4. 3D views for an etching pit observed after EP on fine grain material. Curvature radius on the edges have been measured at several different places and range from 5 to 15 µm on such sharp feature, the ellipse method is probably overestimating the radius.

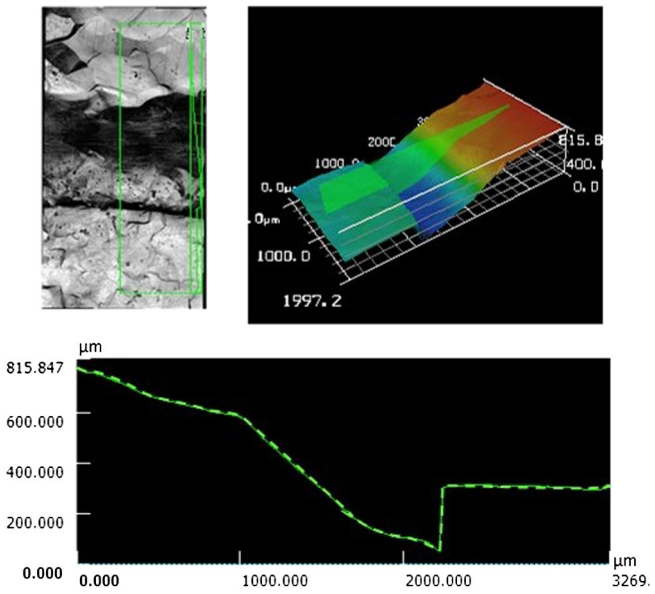

FIG. 5. Welding misalignment. The angles of curvature on the right-hand side of the picture range 15–25 µm (probably overestimated too).Upper panel left: optical image, upper panel right: 3D projection, lower panel: profile view along the green line shown on the upper panels.

III. SIMULATIONS

The purpose of this part is to show how to simulate easily any kind of defect with commercial simulation software, such as Ansys Electromagnetic Desktop. There is no analytical result (contrary to [22,27]), only the results of the simulation are presented.

The first part deals with models of grain using protruding cylinders. Then, an etching pit defect is studied. And finally, a local welding defect is simulated.

A. Grain models

Grains were represented with a very simple cylinder and a fillet. Three parameters can be set: the diameter of the cylinder, called D, the thickness of the cylinder, called T, and the radius of the fillet, R.

Two cases appear (see Fig. 6): if the radius of the fillet is smaller than the thickness, we can clearly see a cylinder with rounded edges. On the other side, if the radius of the fillet is larger than the fillet, the grain looks more like a "dome." In both cases, the diameter of the disc base of the grain is defined by the diameter of the cylinder even if the cylinder is not visible (bottom diagram in Fig. 6).

B. Cavity model

The model of the cavity is a simple pillbox. The size of the pillbox cavity was 100 mm high for a radius of 500 mm. For these dimensions, the eigenfrequency is 230 MHz.

In order to make the simulations faster and easier, only 1/16th of the cavity was simulated (see Fig. 7). The grain defect was located at around 4/5th of the center.

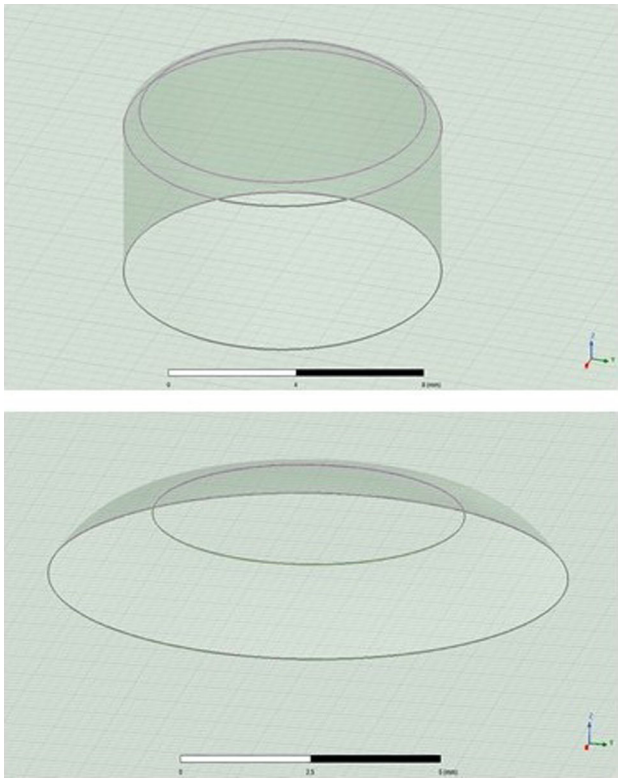

FIG. 6. Two types of grains. Top: the fillet is smaller than the thickness. Bottom: the fillet is larger than the thickness.

Cut surfaces were replaced by perfect magnetic conductors in order to simulate the field of a full pillbox cavity.

C. Software

Simulations were done with HFSS, included in the Electromagnetic Desktop developed by the Ansys Company. This well-known software uses the finite element method for resolution. The typical number of tetrahedrons is around 500 000.

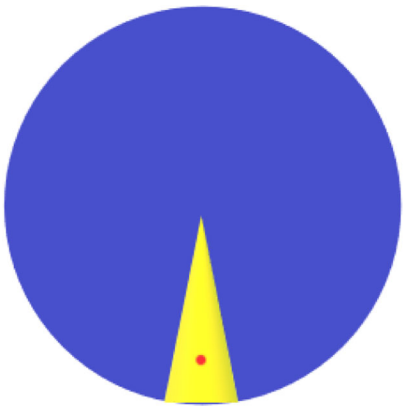

FIG. 7. Pillbox for rf simulations. Only the "yellow part" is simulated, the rest is replaced by perfect magnetic conductor walls.

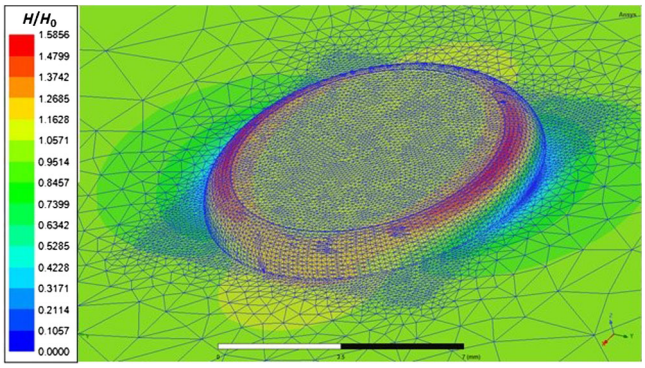

FIG. 8. Example of surface mesh for simulating the effect of the grain.

It is possible to define a "nonmodel" cube where the mesh can be concentrated. In our simulations, we tried to define this cube as close as possible to the grain, in order to maximize the accuracy on the grain surface. See Fig. 8 for illustration.

IV. RESULTS

A. General observations about grains

Figure 8 shows a typical simulated grain, where the highest field is concentrated on the top of the fillet. Figure 9 shows exactly the same grain seen from the top (without representation of the mesh).

The field "far enough" of the grain (typically a few diameters far from the grain), is homogeneous. Two large lobes appear in the direction of the B field (along the Y axis), with a lower field on the deep edge and the highest field on the prominent edge. Two smaller lobes appear perpendicularly to the B field (along the X axis), with a higher field on both deep and prominent edges.

In some rare cases, if the thickness of the grain is high enough (typically more than 25% of the diameter of the grain), the peak field is distributed on the edge of the big lobes (Y axis) and on the sides of the small lobes (X axis). For example, this can be seen in Fig. 10.

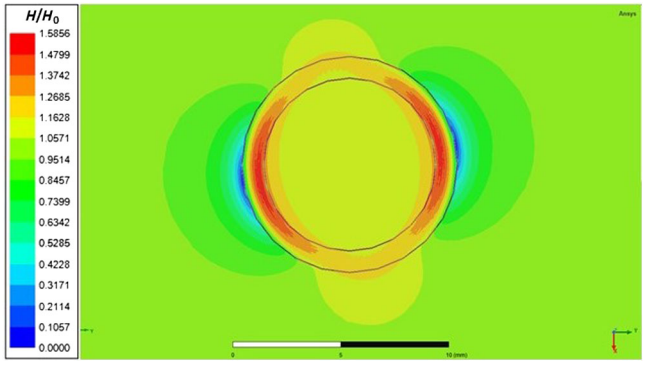

FIG. 9. Grain of Fig. 8 seen from the top, with the mesh. Two large lobes are visible in the Y direction, and two smaller lobes in the X direction.

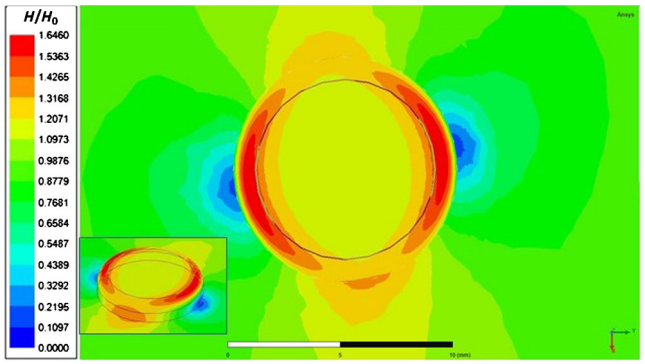

FIG. 10. For higher thicknesses, the peak is similar for both Y and X axes lobes. The thickness of the grain in this case is 20% of the diameter.

Finally, the peak fields appear either on the edge, perpendicular to the B-field, or on the side of the grain, parallel to the B-field, if the thickness of the grain is high enough.

In the next chapters, we tried to estimate the reproducibility of the H_{peak} measurement by getting a few points in the peak field area with different mesh resolutions. In general, the reproducibility was around 2%. Far enough of the defect, the reproducibility is far better (less than 0.5%), as the field is very smooth.

B. Invariances

Before launching a systematic study of these parameters, we tried to study possible invariances. We focused on two invariances: homothety of the defect in the same cavity and homothety of the cavity, with the same defect. The cavity is always the pillbox described in Fig. 7.

The first test was done with a defect with the following dimensions (simulation A in Table II): 80 μm thick, 1000 μm diameter, and 30 μm curvature radius. The defect was enlarged with a factor of 10 (800 μm thick, 10 mm diameter, 300 μm curvature radius, simulation B), and a factor of 30 (simulation C). The three simulations were done with the same pillbox cavity.

Table II shows the measured peak fields for simulations A to C. These simulations show that the homothety of the

TABLE II. List of simulations verifying the homothety and frequency invariances. H_{peak}/H_0 represents the ratio between the peak field on the defect and the average field around the defect. A to C are homothetic defects. D and E are the same defects at different frequencies.

Simulation	Frequency (MHz)	D (μm)	T (μm)	R (μm)	$\frac{H_{\text{peak}}}{H_0}$
A	230	1000	80	30	1.78 ± 0.03
B	230	10 000	800	300	1.77 ± 0.03
C	230	30 000	2400	900	1.80 ± 0.03
D	230	10 000	1000	1000	1.49 ± 0.02
E	1150	10 000	1000	1000	1.49 ± 0.02

defect has no impact on the peak field. If the three dimensions are multiplied by the same factor, the peak field is identical.

The second set of simulations was about modifying the size of the pillbox. For this purpose, we divided all dimensions of the pillbox by a factor of 5. The new frequency is 1150 MHz. As the field was always normalized to a stored energy of 1 J for simulations, the resulting raw field is higher when the cavity is smaller, but it has no consequence on the shape, and on the ratio H_{peak}/H_0.

A defect was defined with dimensions 1 mm thick, 10 mm diameter, and 1 mm curvature radius. It was simulated with the 230-MHz pillbox (simulation D in Table II) and in the 1150 MHz pillbox (simulation E). The position of the defect was modified with the same homothety transform, in order to be in the same area. If we compare the diameter of the defect and the wavelength, we get a ratio $1/130$ for the 230-MHz pillbox and $1/26$ for the 1150 MHz pillbox.

These simulations show that the increase of the field is invariant by homothety of the defect and by homothety of the pillbox, at least if the defect is smaller than about 5% of the studied defect (see Table II). Consequently, it is also invariant by homothety of both the defect and the pillbox. This was tested by a few more simulations.

For the study of the grains, we decided to fix the diameter, to 10 mm, and only study the two other parameters, the thickness and the curvature of the fillet. For the study of the pitting, we also fixed the diameter to 10 mm. This makes the meshing of the defect far easier for the software if the ratio between the defect and the cavity remains "reasonable."

C. Study of grains

The two remaining parameters have been studied for T (thickness) from 0.1 mm (1% of D) to 5 mm (50% of D) and for R (curvature radius) from 0.25 mm (2.5% of D) to 2.5 mm (25% of D). The result is shown in Fig. 11.

D. Fit of the grain simulations

In order to fit the data, we used a linear regression of $\log\frac{H_{\text{peak}}}{H_0}$ as a function of $\log\frac{R}{D}$ and $\log\frac{T}{D}$. The resulting slopes were rounded to the closest half unit. This gives an estimation of the ideal exponent for each of these parameters: -1 for $\frac{R}{D}$ and ½ for $\frac{T}{D}$.

Finally, $\frac{H_{\text{peak}}}{H_0}$ was fitted with a linear regression in $\frac{D}{R}$, $\sqrt{\frac{T}{D}}$ and the cross factor $\sqrt{\frac{DT}{R}}$ in order to estimate the correlation between both parameters:

$$\frac{H_{\text{peak}}}{H_0} \simeq 1 + 0.0073 \times \frac{D}{R} + 0.83 \times \sqrt{\frac{T}{D}} + 0.028 \times \frac{\sqrt{DT}}{R}. \quad (1)$$

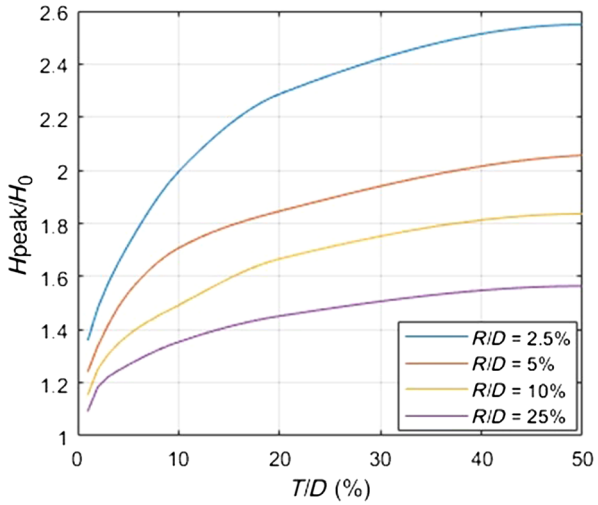

FIG. 11. H_{peak}/H_0 simulated for different grain sizes with "BCP" characteristics.

With this estimation, it is possible to represent the different grains described in Table I. The contour map background from Figure 17 follows equation (1) at the end of the paper. The value of H_{peak}/H_0, calculated after the experimental measurements from Table I is also indicated in the same figure.

E. Etching pit

The last simulation is for the etching pit. It was modeled with a hollow in the cavity (instead of a bump like for grains). The parameters are the fillet radii and the thickness. We tried to mimic the observation shown in Fig. 4 but with a cylindrical symmetry. The 1150 MHz cavity was used for this simulation.

The simulation was done with a diameter of the etching pit of 200 μm, a hole depth of 20 μm, and a fillet radius of 5 μm. If we apply these parameters to the previous model for grains (replacing the thickness in the formula with the depth of the pit), the estimated formula for H_{peak}/H_0 gives 1.90.

Figure 12 presents the result given by the simulation. The simulated ratio H_{peak}/H_0 was measured at 2.01 ± 0.04, i.e., the same field enhancement magnitude, even if the shape is different and peak fields are on different positions. This demonstrates that the previous formula can also be used for etching pits after having estimated a typical radius, depth, and fillet.

These field enhancement levels are comparable to other estimations on pits as published in [22,25,27] and in chapter 3 in [38].

As shown in Fig. 1 and references from this chapter, etching pit often occur in areas where walls of dislocation have accumulated, which is often encountered in the presence of damage or remaining thermal strain. The presence of a pit in the equator area of the cavities is a

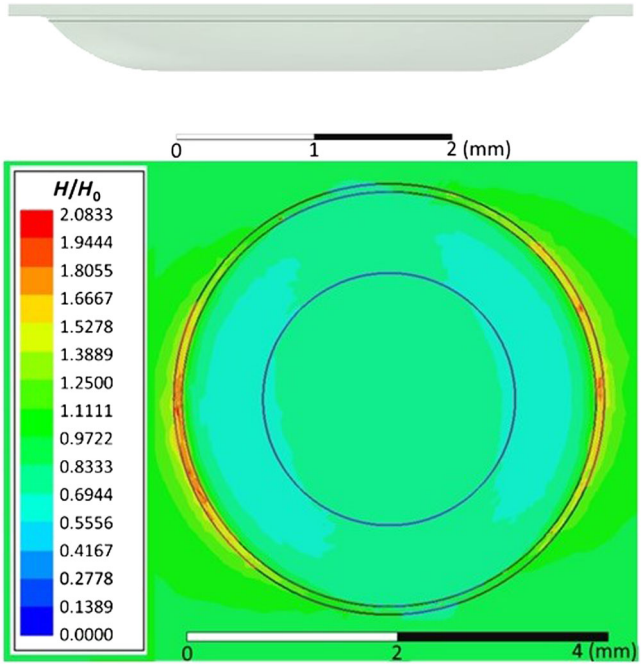

FIG. 12. Etching pit: model (top) and result (bottom).

strong indication that the fabrication needs to be more closely monitored.

F. Large defect

In this last part, we studied a large defect. Here, we considered the case of a welding defect, as shown in Fig. 5.

In order to simulate this defect, we considered the print caused by a tilted cylinder in the cavity. In the simulation software, the cavity is always represented by one 16th of a cylinder, filled with vacuum, with perfect electric conductor borders. In this part of the cylinder, another smaller cylinder is drawn, filled with vacuum. The bottom of this

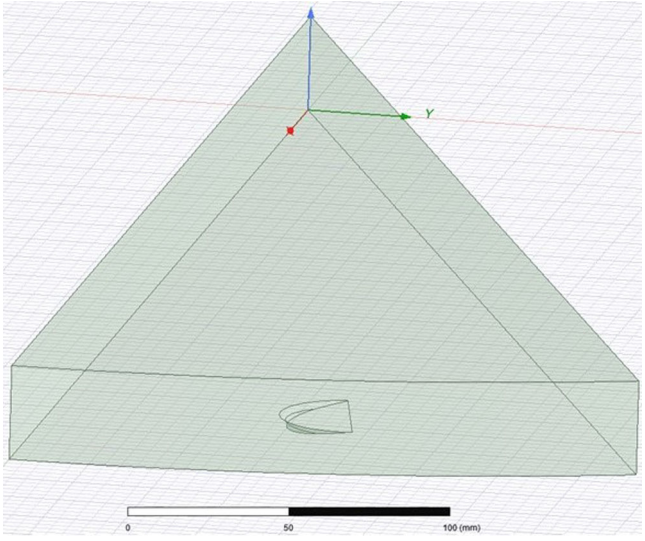

FIG. 13. Example of the large defect as simulated with HFSS.

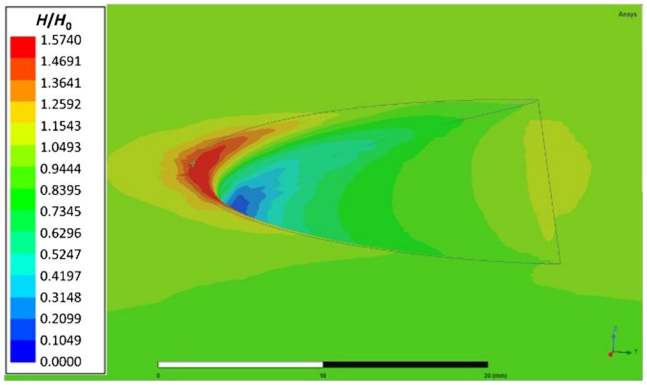

FIG. 14. Result of the simulation of Fig. 13. The depth is here 3.5 mm, and the fillet radius is 2 mm. The peak ratio is 1.6.

smaller cylinder is at the same level as the bottom of the cavity. Then, this smaller cylinder is tilted by a very small angle (typically less than 10°), creating a gap on the tilted side. The edge is smoothed with a fillet radius. Figure 13 shows an example with a 10° tilt.

For this large defect, one parameter is fixed: the diameter of the tilted cylinder: 40 mm. The cavity is the 230-MHz cavity.

Two parameters can be changed: the tilt angle and the fillet radius. For making illustrations easier, instead of the tilt angle, we will use the maximal depth of the defect to describe it. It can be roughly estimated by depth $\simeq \text{angle}_{\text{tilt}}[\text{rad}] \times 20$ mm.

In the following paragraphs, the depth is represented by the letter Δ.

As previously, we tried to observe invariances. Simulations were done with the same cylinder diameter (40 mm) and with parameters presented in Table III. The resulting peak ratios are almost identical.

Thus, contrary to the previous invariances with grains, H_{peak}/H_0 is almost invariant by multiplying the depth and the fillet radius by the same coefficient, even when keeping the same cylinder diameter. This shows that, for very large defect diameters, the diameter does not significantly affect the peak ratio. Thus, the formula for grains certainly reaches a limit when the size of the grain is too big.

In our case, with simulations for Δ/R ratios from 1.7 to 11.6, we got the following estimated formula:

$$\frac{H_{\text{peak}}}{H_0} \simeq 1 + 0.43\sqrt{\frac{\Delta}{\mathrm{R}}}. \tag{2}$$

TABLE III. List of simulations with large defect. F and G are homothetic defects.

Simulations	Frequency (MHz)	Δ (μm)	R (μm)	$\frac{H_{\text{peak}}}{H_0}$
F	230	1000	300	4.51
G	230	3350	1000	4.80

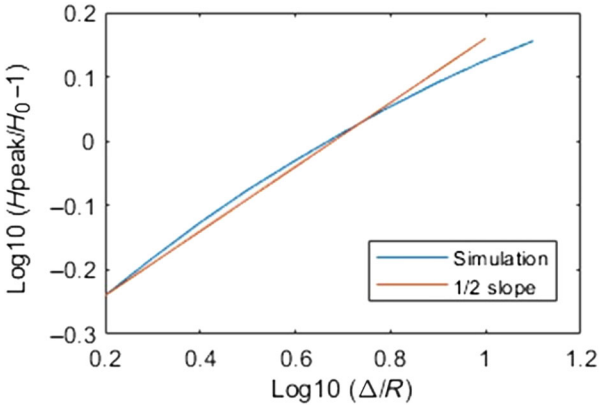

FIG. 15. Log-log figure of $\frac{H_{\text{peak}}-H_0}{H_0}$ as a function of $\frac{\Delta}{R}$. The orange plot represents Eq. (2) and the blue plot represents the simulation with Ansys.

The square root in (2) was estimated with the log-log regression rounded to the half unit, as illustrated in Fig. 15. The 0.43 factor was estimated by regression of $\frac{H_{\text{peak}}}{H_0}$ as a function of $\sqrt{\frac{\Delta}{R}}$.

For the welding defect of Fig. 5, the depth, Δ, is around 200 μm, and the fillet radius, R, is around 20 μm. The diameter of the weld was around 40 mm. The formula gives a peak ratio of around 2.4. The defect was represented in Fig. 17 with these parameters, even if the grain model of Eq. (1) does not really apply to this kind of defect.

The test of the cavity with this welding defect showed a quench at 5.2 MV/m. At this accelerating field, the theoretical surface peak field is 55 mT, without defect. If we apply a 2.4 factor to this surface peak field, we obtain a real surface peak field of around 130 mT. Tests with temperature probes showed that the quench came from this defecting weld. This tends to validate the model as the expected maximal magnetic field is close to 150 mT for rf fields at 4.2K.

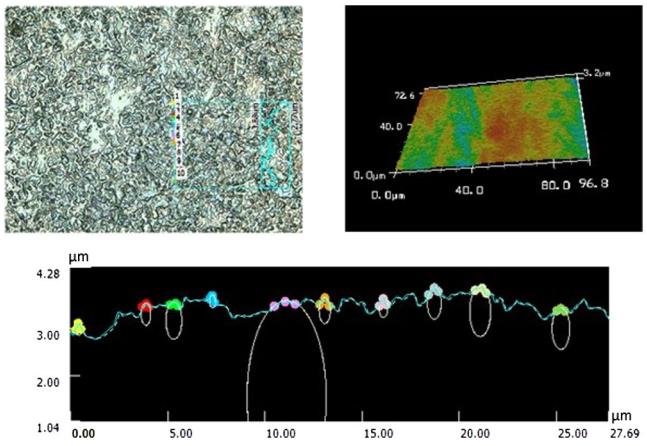

FIG. 16. Surface characteristics of the Nb_3Sn Sample. Roughness Sk is only 0.42 μm. Upper panel left: optical image, upper panel right: 3D projection; lower panel: profile view along the blue line shown on the upper left panel, with an example of curvature angle determination.

G. Thin films

As shown earlier, homothety does not change the field enhancement factor. Thin films present small grains and small thicknesses (so small roughness parameters), but the

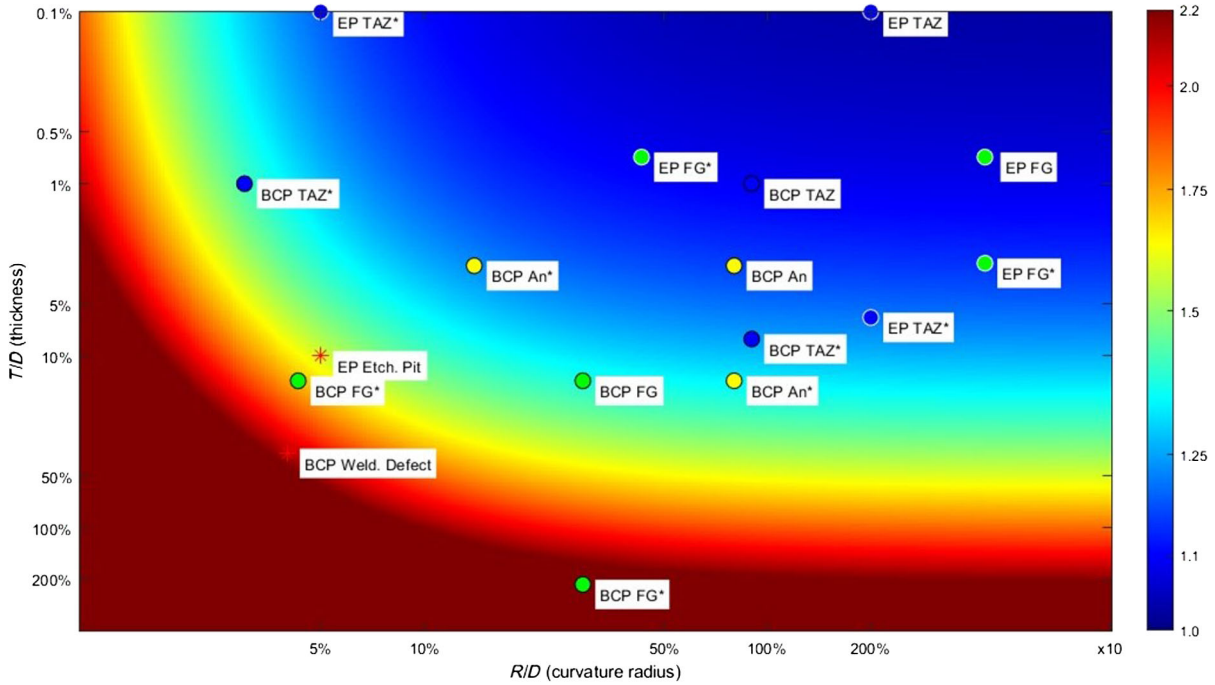

FIG. 17. Contour map along Eq. (1) and calculated H_{peak}/H_0 for the measured values exposed in Table I. For comparison, large defects and thin film values have been added to the plot although they do not follow Eq. (1).

TABLE IV. H_{peak}/H_0 calculated for two thin film samples (see measured characteristics in Table I). Surface measurement of the Nb_3Sn sample is shown in Fig. 16.

Material	Sample	$\frac{H_{\mathrm{peak}}}{H_0}$
Nb/Cu	From CERN	1.59
Nb_3Sn	From Cornell	1.42

shape of the grain is what matters. Indeed, the field enhancement factor calculated for two different thin films (taken at random) is around 1.5 (see Table IV), which shows that this aspect of things should be explored more thoroughly.

V. CONCLUSION

In this paper, we propose a model of field enhancement calculation that allows predicting the impact of surface morphology as measured in realistic conditions (roughness after surface polishing on small grain, annealed and TAZ affected Nb, representative defects like etching pit of welding defect, and thin film surfaces).

One can observe that for EP surfaces, mean values of surface roughness as well as extreme values do not enhance particularly the local field: enhancement keeps below 10%. For BCP surfaces, on the other hand, singular value can produce very high local field enhancement, in particular, on BCP fine grains. The model definitively assesses that premature quench can result from a local defect and that the risk is not negligible.

Large defects like etching pit or welding defects exhibit a very large calculated H_{peak}/H_0, which is corroborated by the fact that the cavities where those defects have been measured indeed presented a very early quench. These results confirm that a better monitoring of fabrication steps is needed, in particular, checking that the damaged layer has been fully removed and that the cooling condition after welding minimizes the risks of thermal strain.

Finally, we show indication that thin films, although they exhibit small roughness, due to the homothety invariance, can also be subjected to early quenches due to morphologic defects. We plan to study this aspect in more detail in a further publication.

We hope this simple model can help to define better surface finishing requirements for projects and help to analyze the impact of fabrication defects.

Most of the calculated field enhancements have been gathered in Fig. 17 for comparison purposes.

[1] S. Berry *et al.*, Topologic analysis of samples and cavities: A new tool for morphologic inspection of quench site, in *Proceedings of 11th Workshop on RF Superconductivity, SRF2003, Lübeck/Travemünder, Germany* (JACoW, CERN, Geneva, 2003), p. 591, https://accelconf.web.cern.ch/SRF2003/papers/thp04.pdf.

[2] T. Kubo, Superfluid flow in disordered superconductors with Dynes pair-breaking scattering: Depairing current, kinetic inductance, and superheating field, Phys. Rev. Res. **2**, 033203 (2020).

[3] F. P.-J. Lin and A. Gurevich, Effect of impurities on the superheating field of Type II superconductors, Phys. Rev. B **85**, 054513 (2012).

[4] M. K. Transtrum, G. Catelani, and J. P. Sethna, Superheating field of superconductors within Ginzburg-Landau theory, Phys. Rev. B **83**, 094505 (2011).

[5] D. Reschke, V. Gubarev, J. Schaffran, L. Steder, N. Walker, M. Wenskat, and L. Monaco, Performance in the vertical test of the 832 nine-cell 1.3 GHz cavities for the European X-ray Free Electron Laser, Phys. Rev. Accel. Beams **20**, 042004 (2017).

[6] R.-L. Geng *et al.*, World record accelerating gradient achieved in a superconducting niobium RF cavity, in *Proceedings of the 21st Particle Accelerator Conference, Knoxville, TN, 2005* (IEEE, Piscataway, NJ, 2005), p. 653.

[7] B. Visentin *et al.*, A non-electropolished niobium cavity reached 40 MV/m at Saclay, in *Proceedings of the 8th European Particle Accelerator Conference, Paris, 2002* (EPS-IGA and CERN, Geneva, 2002), p. 2292.

[8] T. Kubo *et al.*, In-house production of a large-grain single-cell cavity at cavity fabrication facility and results of performance tests, in *Proceedings of of the 5th International Particle Accelerator Conference, IPAC 2014, Dresden, Germany, 2014* (JACoW, Geneva, Switzerland, 2014), p. 2519.

[9] S. Posen, N. Valles, and M. Liepe, Radio frequency magnetic field limits of Nb and Nb_3Sn, Phys. Rev. Lett. **115**, 047001 (2015).

[10] T. Yogi, G. Dick, and J. Mercereau, Critical rf magnetic fields for some type-I and type-II superconductors, Phys. Rev. Lett. **39**, 826 (1977).

[11] T. Hays and H. Padamsee. Measuring the RF critical field of Pb, Nb, Nb_3Sn, in *Proceedings of SRF 97. Abano Terme (Padova), Italy* (JACoW, CERN, Geneva, 1997), p. 789.

[12] K. Saito. Surface smoothness for high gradient Nb SRF cavities, in *Proceedings of SRF2003, Lübeck/Travemünder, Germany* (JACoW, CERN, Geneva, 2003), p. 637.

[13] D. Y. Vodolazov, I. Maksimov, and E. Brandt, Vortex entry conditions in type-II superconductors: Effect of surface defects, Physica (Amsterdam) **384C**, 211 (2003).

[14] A. Gurevich, personal communication.

[15] J. Knobloch *et al.*, High-field Q slope in superconducting cavities du to magnetic field enhancement at grain boundaries, in *Proceedings of SRF1999, La Fonda Hotel, Santa Fe, NM* (JACoW, CERN, Geneva, 1999), p. 77.

[16] S. Berry, C. Antoine, and M. Desmons. Surface morphology at the quench site, in *Proceedings of the 9th European Particle Accelerator Conference, Lucerne, 2004* (EPS-AG, Lucerne, 2004), p. 1000.

[17] Y. Iwashita, Y. Tajima, and H. Hayano, Development of high resolution camera for observations of superconducting cavities, Phys. Rev. ST Accel. Beams **11**, 093501 (2008).

[18] X. Zhao *et al.*, Study of etching pits in a large-grain single cell bulk niobium cavity, in *Proceedings of SRF2009, Berlin, Germany* (JACoW, CERN, Geneva, 2009), p. 446.

[19] T. Kubo *et al.*, Study on optimum electron beam welding conditions for superconducting accelerating cavities, in *Proceedings of SRF2013, Paris, France* (JACoW, Geneva, 2013), p. 424.

[20] M. Ge, G. Wu, D. Burk, J. Ozelis, E. Harms, D. Sergatskov, D. Hicks, and L. D. Cooley, Routine characterization of 3D profiles of SRF cavity defects using replica techniques, Supercond. Sci. Technol. **24**, 035002 (2011).

[21] Y. Yamamoto, Cavity diagnostic system for the performance test of the 1.3 GHz superconducting 9-cell cavity, Nucl. Instrum. Methods Phys. Res., Sect. A **623**, 579 (2010).

[22] V. Shemelin and H. Padamsee, Magnetic field enhancement at pits and bumps on the surface of superconducting cavities, TTC-Report 2008, Tesla Technology Collaboration, 2008, https://flash.desy.de/reports_publications/tesla_reports/tesla_reports_2008/.

[23] Z. Insepov and J. Norem, Can surface cracks and unipolar arcs explain breakdown and gradient limits?, J Vac. Sci. Technol. A **31**, 011302 (2013).

[24] G. Wu *et al.*, Investigations of surface quality and SRF cavity performance, arXiv:1206.6331.

[25] Y. Xie and M. Liepe, New Insights Into Quench Caused by Surface Pits in SRF Cavities, in *Proceedings of SRF2013, Paris, France* (JACoW, CERN, Geneva, 2013), p. 378.

[26] Y. Xie, M. Liepe, and H. Padamsee, Quench simulation using a ring-type defect model, in *Proceedings of SRF2011, Chicago, IL USA* (JACoW, CERN, Geneva, 2011).

[27] T. Kubo, Magnetic field enhancement at a pit on the surface of a superconducting accelerating cavity, Prog. Theor. Exp. Phys. **2015**, 073G01 (2015).

[28] H. Tian, G. Ribeill, C. Xu, C. E. Reece, and M. J. Kelley, A novel approach to characterizing the surface topography of niobium superconducting radio frequency (SRF) accelerator cavities, Appl. Surf. Sci. **257**, 4781 (2011).

[29] H. Tian, Surface roughness characterization of niobium subjected to incremental BCP and EP processing steps, in *Proceedings of SRF2007, Beijing, China* (JACoW, CERN, Geneva, 2007), p. 438.

[30] C. Xu, C. E. Reece, and M. J. Kelley, Simulation of nonlinear superconducting rf losses derived from characteristic topography of etched and electropolished niobium surfaces, Phys. Rev. Accel. Beams **19**, 033501 (2016).

[31] Y. Morozumi, Realistic evaluation of local field enhancement based on precision profilometry of surface defects, in *Proceedings of IPAC10, Kyoto, Japan* (JACoW, CERN, Geneva, 2010), p. 2932.

[32] E. M. Gutman, *Mechanochemistry of Materials* (Cambridge International Science Publishing, Cambridge, 1998).

[33] E. Zedier, Etching phenomena in the {111} plane of niobium, J. Appl. Phys. **38**, 2046 (1967).

[34] P. Evans, Dislocation etch pit studies in annealed and deformed polycrystalline niobium, J. Less Common Metals **6**, 253 (1964).

[35] Y. Arata, K. Terai, and S. Matsuda, Study on characteristics of weld defect and its prevention in electron beam welding (Report I): Characteristics of weld porosities, Trans. JWRI **2**, 103 (1973).

[36] L. Cooley *et al.*, Impact of forming, welding, and electropolishing on pitting and the surface finish of SRF cavity niobium, IEEE Trans. Appl. Supercond. **21**, 2609 (2010).

[37] F. Eozénou *et al.*, Efficiency of electropolishing vs bath composition and aging: First results, in *Proceedings of SRF2005. Cornell University, Ithaca, NY* (JACoW, CERN, Geneva, Switzerland, 2005), p. 451.

[38] C. Z. Antoine, Materials, and surface aspects in the development of SRF niobium cavities, in *EuCARD Editorial Series on Accelerator Science, and Technology*, edited by J. P. Koutchouk and R. S. Romaniuk (European Project EUCARD, Geneva, 2012), Vol. 12.